# Modeling heat flux in the Beaufort Gyre between 2016 and 2019.

Jullian C. B. Williams
NASA Center for Advanced Measurements in Extreme Environments, Kleese College of Engineering, The University of Texas at San Antonio, 1 UTSA Circle, San Antonio, Texas 78249.

## Abstract

Leads are a primary component of heat flux during polar night-time in the Arctic Ocean. During the winter, there is negligible shortwave radiation incident on the ice surface. Instead, open water and thin ice lead formations on the ice are the primary contributors of longwave radiation. In fact, open water leads produce turbulent heat flux up to 600 W.m$^{-2}$ while multi-year ice is typically less than 5 W.m$^{-2}$ (Maykut, 1982). This paper models and compares net heat flux over sea ice using ERA5 monthly averaged reanalysis data with intramonthly lead fractions for the winter months between 2016 and 2019.

## Introduction

The thermodynamics surrounding Arctic sea ice is a prolific area of research with increasing application in the global climate change problem. Polar latent and sensible heat flux are driving forces regarding the change in sea ice cover and dynamics (Bourassa et al., 2013). Vertical heat exchange from the ice layer to the atmosphere's boundary layer control the changes in energy available in high latitude regions during Polar nighttime. Bourassa et al. (2013), describe heat flux as a function of strong katabatic winds, sea ice lead prevalence and orientation, the presence of polynyas, deep water formation, circulation, freshwater input from snow and air-sea temperature changes. In the Beaufort gyre, there is an observed reduction in the volume of thickness of pack ice over the past 35 years (Hutchings et al., 2008, Parkinson and

Cavalieri, 2002; Comiso 2002, Wadhams and Davis, 2000; Tucker et al., 2001; Rothrock et al., 1999) and has impacted changes in sea ice processes and features such as ice-albedo (Ackley et al., 2020, Rösel et al., 2011, Miao et al., 2015, Tschudi et al., 2008, Perovich 1996 and 2002) as well as the growth and extent of open water features such as polynyas and melt ponds (Macdonald et al., 2023, Dai et al., 2020, Scharien et al., 2017) and leads (Lohse et al., 2019, 2020 and 2021, Willmes and Heinemann, 2015, Brohan and Kaleschke, 2014, Röhrs and Kaleschke, 2012, Lindsay and Rothrock, 1995).

Heat regulators in the Arctic such as leads (Li et al., 2020) facilitate energy and gaseous exchange (Gosink, 1976 and DeLille et al., 2014) during Polar night-time in the Arctic and contribute to the global climate by influencing atmospheric exchanges. Open water and newly frozen leads account for the first and second-largest heat fluxes in the atmosphere, producing boundary layer clouds (Li et al., 2020, Marcq and Weiss, 2012, Maykut 1982). In contrast, the lowest heat exchanges occur over thick ice areas (Li et al., 2020). Studying the changes in heat flux over the Arctic and Antarctic is critical as increasing evidence of reductions in ice sheets, glacier mass balance and snow cover are recorded (Lemke et al., 2007).

The Beaufort Gyre has a clockwise oscillation, that sits North and West of the Alaskan coastline and Banks Island, respectively (Talley 2011). This movement of the ocean provides typically, an eastward movement of ice from the Gyre into the larger Arctic Ocean. However, the Beaufort Gyre is also known to revert to an anti-clockwise motion, concentrating the newly formed ice in the opposite direction. Heat exchange from the sea ice surface to the atmosphere is observed in this study, during the mid-winter seasons in the Beaufort Sea. Li et al., (2020) describe the change in heat flux over a 6-hour timeframe with respect to changes in lead type. In this study, we calculate heat flux as described by Cheng et al., (2017) to illustrate the change in heat flux. Understanding the changes in heat flux can provide further motivation to study sea ice changes with respect to global change and climate studies.

**Study area**

The study area is approximately 300 miles offshore Barrow, Alaska into the Beaufort Sea area. The Beaufort Sea is approximately 500,000 km$^2$ in surface area and roughly located ~70 – 75° N and 120-160 °W in the Arctic Ocean (Figure 1). The boundaries of the wedge-shaped geometry of the Beaufort Sea are flanked in the West nearby Point Barrow, in the east by Banks Island, and the lower Canadian Archipelago while fixed against the coast of the Alaskan and Canadian boundaries. The northern edge of the Beaufort Sea is a straight-line edge leading near Point Barrow to the Southern tip of Prince Patrick Island. This area was selected as an optimal lead energy flux area as described by Li, et.al, (2020) and suggests an estimate of net heat flux over the Beaufort Gyre shown in Figure 2. According to the United States Census Bureau, this region is roughly 1,300 miles south of the North Pole and 320 miles north of the Arctic Circle, resulting in a cold and dry polar climate. Barrow itself, is a tundra environment characterized largely by permafrost that is proximately 1,300 feet in depth.

The upwelling of ocean currents allows heat, gas and moisture exchange fluxes between the ocean and atmosphere over the studied area. This is one of the influences of heat exchange by way of thermal ocean currents that cause temperatures in the Arctic to be generally warmer than those in the Antarctic. This unique dynamic is a point of interest for studying thermodynamics in the Arctic.

*Figure 1: The Beaufort Sea location in the heat flux study denoted in dark green adapted from Yang et al., 2023.*

*Figure 2: Heat flux estimates from midwinter Arctic leads form and dissipate low clouds in Li et al. (2020).*

## Data and Methods

We calculate the net heat flux over the Beaufort Gyre described by Cheng et al., (2017) as Q (in $W.m^{-2}$) in the Beaufort Gyre using the near-surface atmospheric input data as monthly averaged air temperature at 2m, dewpoint temperature at 2m, windspeed and vector winds at 10m from ERA reanalysis data with spatial resolution of 0.25° x 0.25° where:

$Q = -L_o + F_s + F_e$ eq. 5.

Where $L_o$ is the upward thermal radiation and $F_s$ and $F_e$ are the sensible and latent heat flux.

$L_o$ is calculated using the Stefan-Boltzmann Law where:

$L_o = \varepsilon\sigma T_0$ eq. 6.

Where ε is the longwave emissivity of open water (0.99), σ is the Stefan-Boltzman constant (5.67 x10-8 $W^{-2}.K^{-4}$) and $T_0$ is the freezing point of seawater at the water surface (Ts, in K.)

$T_0 = Ts = 273.15-0.0137-0.05199sw – 0.00007225sw$ eq. 7.

Where sw (in %) is the salinity of sea water, estimated at 34%.

Sensible (Fs) and latent heat flux (Fe) are calculated by:

$Fs = \rho_a C_p C_s U(T_a-T_0)$ eq. 8.

And

$Fe = 0.622\rho_a L_v C_e U(re_a-e_s)/P_0$ eq. 9.

Where $\rho_a$ is the density of air at standard atmospheric pressure at 0°C, taken as 1.3 $kg.m^{-3}$, Cp is the specific heat of air at constant pressure, taken as 1004 $J.kg^{-1}.K^{-1}$, U (in $m.s^{-1}$) is the windspeed at 10-m, and Ta (in K) is the air temperature at 2 m both taken from the processed ERA5 data. $C_s$ and $C_e$ are bulk transfer coefficients for sensible and laten heat respectively, both assumed at 0.00144. $P_0$ (in pa) is the surface air pressure, $L_v$ (in $J.Kg^{-1}$) is the latent heat of water vaporization, r is the relative humidity, $e_a$ (in pa) is the saturation water vapor pressure at the air temperature, $re_a$ is the actual water vapor of the air and $e_s$ is (in pa) is the saturated water vapor pressure at the surface temperature and are calculated as:

$$Lv = (2.501 - 0.00237(Ts - 273.15)) * 10^6 \quad \text{eq. 10.}$$

$$e_s = 611.21 * 10^{(9.8094*(T0 - 273.15)/(T0 + 0.71))} \quad \text{eq. 11.}$$

$$re_a = 611.21 * 10^{(9.8094*(Td - 273.15)/(Td + 0.71))} \quad \text{eq. 12.}$$

where Td is the dewpoint temperature taken from the ERA5 processed data. In this study, we use the10-m windspeed and 10-m vector components to estimate the net heat flux which can over or underestimate the model.

**Results and discussion**

The Beaufort Gyre is dynamic with a heat circulatory system (Figure 3) that periodically expresses reversals in rotation. For example, the figure shows that there is a strong change in higher heat concentrations from the western and south-western to eastern flanks of the gyre between December 2017 to February 2018. However, there appears to be smaller variations in heat flux between December 2016 with respect to January and February 2017. The figure shows yearly changes in heat flux where higher heat exchange is expressed in the south-eastern segment of the gyre in December 2016, then from the western flank in December 2017 and back again from the south-east, offshore Bank's island in December 2018. A similar relationship exists in the January plots. In January, the heat concentration remains higher from the western bank of the gyre in 2018 to 2019 instead of returning to higher concentration towards the south-east as in

December 2016-2018. However, in 2017 the higher concentration of heat flux is towards the south-west of the gyre in February, but the concentration becomes higher towards the east of the gyre in February 2018 and 2019. The gyre also displays intramonthly reversals of heat concentration. In December 2016, the gyre's high heat flux is towards the south-east until January 2017 which then changes towards the south-west in February 2017. In December 2017, the gyre shows a strong high flux from its western edge until January 2017. This changes towards the east by February 2018. The gyre then shows its highest flux again towards the south-east of the gyre in December 2018. However, the gyre changes to high concentrations in January 2019 from the west and then returns to high concentration from the south-east in February 2019.

*Figure 3: Heat flux changes in the Beaufort Gyre for the winter periods December to February from 2016-2019.*

The gyre may demonstrate small and large scale systems that influence the rate of heat flux across the basin. West of Bank's island is the Fram Strait where a polynya opens at the height of the winter period of the Gyre. This pervasive open water feature is a source of high heat flux, driving up the total rate of flux. However, the changes in heat flux each year express a more complex system, that is not readily described by the strait or other nearby polynyas.

***Spatial distribution of net heat flux across the Beaufort Gyre***

The net heat flux estimated using the 10m vector and windspeed can be compared to the ERA5 derived net flux as a ground truth. Figure 4a-c shows the ERA5 derived net heat flux for the winter period taken December – February for the years 2016 – 2019 alongside the calculated heat fluxes for the same time series using the 10m vector wind and windspeed components in the Beaufort Sea.

The ERA5 results show the changes in net heat flux over the Beaufort Sea throughout the winter period for the time series. The derived results show the calculated net flux as described in the method. While the range of values coincide between themselves as well as that reported in Li et al., (2020), the spatial distribution of flux in each month across the years differ.

The 10m vector wind estimate of net flux in December 2016 (Figure 4a) shows lower heat flux within the scope of the ERA5 data. The 10m windspeed estimate shows higher net flux over the Beaufort Sea. However, both the 10m vector estimate and ground truth suggest higher fluxes towards the northerly segments of the gyre. In contrast, the 10m windspeed estimate shows its lowest flux towards the north in the gyre. By December 2017, the calculated estimates show agreement in high concentration distribution across the gyre with higher flux across the central, west-east segment of the gyre. The calculated flux in December 2017 shows their highest concentrations to the west of the gyre, while the ground truth shows its highest flux to the north-east. On the other hand, the gradient of the heat flux decreases towards the north-east in the calculated estimates.

*Figure 4a: Net heat flux for December 2016 – 2019 over the Beaufort Sea using ERA reanalysis data with ERA5 net heat fluxes, 10m windspeed and 10m vector wind estimates from 2016 – 2019.*

*Figure 4b: Net heat flux for January 2016 – 2019 over the Beaufort Sea using ERA reanalysis data with ERA5 net heat fluxes, 10m windspeed and 10m vector wind estimates from 2017 – 2019.*

*Figure 4c: Net heat flux for February 2016 – 2019 over the Beaufort Sea using ERA reanalysis data with ERA5 net heat fluxes, 10m windspeed and 10m vector wind estimates from 2017 – 2019.*

In December 2018 (Figure 4a), the heat flux gradient increases toward the north-east as well, however, the calculated flux estimates do not show similar stratification. Instead, the flux is higher and lower in the south-eastern segment of the Beaufort gyre in the 10m windspeed and vector respectively. The December 2018 estimate in the 10m vector shows a concentration of higher flux in a strong west-east orientation while the 10m windspeed shows stratification of the flux gradient increasing towards the south. The ground truth in December 2018 however, shows the highest flux towards the north-east, in disagreement with the calculated estimates.

Finally, in December 2019, the ground truth shows high heat flux in the north of the gyre and lower flux towards the south. There is a small increase just south of Bank's Island to the south-east of the gyre. This small increase appears more southerly in the calculated estimates. However, the 10m windspeed estimate shows a more northerly concentration of high net flux while this is shown in a more north-westerly direction in the 10m vector estimate. The 10m windspeed and ground truth show a lower net flux in the north-west segment of the gyre, contrasting the spatial distribution in the 10m vector estimate.

In January 2017 (Figure 4b), the ground truth and 10m vector estimate show higher net flux towards the northern segments of the gyre. The 10m windspeed contrasts that, showing a stronger concentration of higher flux to the southern segment of the gyre. This changes in January 2018, where the ground truth shows lower flux to the west to south-west of the gyre, while the calculated estimates show higher flux in that area. This result continues in January 2019, however, the net flux is higher in distribution than that of January 2018.

February 2017 shows agreement among the ground truth and the calculated estimates where the reduction of net flux is concentrated towards the south-eastern segment of the gyre. However, the ground truth shows higher flux across the northern boundary of the gyre while the 10m windspeed shows its highest flux towards the south-western edge of the gyre. The 10m vector estimate shows a north-east to south-west distribution of high heat flux in the gyre with the highest concentrations towards the north-east and its lowest concentrations towards the north-west. The 10m windspeed estimate also shows a north-east to south-west distribution of higher heat flux, however, the lower concentration is in the opposite direction, towards the north-east.

February 2018 (Figure 4c) shows an even greater disagreement of net flux estimate from the ground truth with respect to the calculated estimates. The calculated estimates show strong high net flux towards the east of the gyre. The ground truth shows a similar spatial change, however, the total flux does not exceed 450 $W.m^{-2}$ in the east. In addition, a strong north-east to easterly lower flux concentration across the gyre that does not appear as concentrated in the calculated estimates. In addition to this, the highest net flux in the ground truth is shown in the most north-western point of the gyre. This is illustrated as the lowest net flux in both calculated estimates. However, by February 2019, the highest flux is shown towards the north-east of the gyre in both the ground truth and 10m vector wind estimates. While the 10m vector estimate and the ground truth show an intrusion of lower flux from the west to the east of the gyre, the 10m windspeed does not show this orientation. Instead, the 10m windspeed estimate shows lower net flux towards the north of the gyre and high flux towards the southern edge of the gyre.

While the 10m vector can be used to estimate the net flux across the Gyre, the 10m windspeed estimate is commonly used to derive the total net flux. Still, neither the 10m windspeed nor the 10m vector estimates consistently show similarity in distribution with the ERA5 estimate or each other. To capture a true representation of the net flux in the gyre, it would be useful to derive glider data to retrieve in-field measurements.

***Net heat flux changes through the winter periods 2016-2019***

The Winter period in the Arctic in this study is denoted from December to February. Using the ground truth, ERA5 derived net flux over the Beaufort gyre shown in figure 5, the net heat flux during winter shows higher concentrations in the north to north-eastern segments of the gyre consistently. However, there are smaller changes over the years at the frost onset (December) and frost maximum (February) in the gyre. Since the high net flux is strongly related to the prevalence of open water leads and polynyas in the gyre, we can suggest that these areas are dominated by these features.

Figure 5 shows the December 2017 heat flux with high flux towards the northern edge of the gyre. However, there is a plume of high flux towards the south-western edge of the gyre appearing in January 2017. This plume is shown in January and February 2017 while increasing in size, as well as in January 2018. The south-western edge of the Beaufort Sea into the Chukchi Sea is flanked with polynyas (Martin 2019). These polynyas are new ice generating areas in the Beaufort, producing juvenile ice that later congeals and consolidates in the Arctic Ocean. In December 2017, high net flux is shown in the north-eastern segment of the gyre while lower flux occurs to the south-east. However, by January and February 2017, the high flux is distributed across the north to north-western edge of the Beaufort while maintaining lower flux towards the south-east. With the clockwise movement of the gyre, the new, thin ice is formed near the coast of Alaska, and moved towards the Chukchi Sea alongside the transpolar drift. As the ice congeals, becoming thicker ice at the height of the winter, ice kinematics allows the formation of leads towards the northern segments of the Beaufort gyre. This behaviour continues in 2018, where in December 2018, the high flux is concentrated to the north-eastern segment of the gyre. Still, a small area of high flux is shown to the most north-western tip of the gyre from December to February 2018. In December 2019, the high flux has switched to the north to north-western segment of the gyre. However, the high flux is seen primarily to the north-east of the gyre in January and February 2019 with a small area of high flux to the north-west. The Beaufort gyre is also known to revert to an anticlockwise rotation against the transpolar drift and demonstrates this here. The total heat flux over the Beaufort Sea during the 2016-2019 period shows the cyclical movement and its reversal of the gyre.

*Figure 5: Net heat flux for December to February (2017 – 2019) over the Beaufort Sea using ERA5 reanalysis net heat flux data.*

**Conclusions**

The Beaufort gyre shows dyanmic changes in its net heat flux over the 2016-2019 period. When comparing the results of the ground truth ERA5 derived net flux to the 10m windspeed and vector wind results, the calculated estimates show similarities and differences with each other and the ground truth data. While the range of total flux is congruent, the spatial distribution of net flux is highly variable across the models. Of course, the simplicity of the heat flux calculations are expected to yield very generalized results. However, there are some spatial disparities with the recommended 10m windspeed that are incongruent with the 10m vector wind and ERA5 ground truth data. While both calculated results appear to show variation in the net flux when compared to the ground truth, the 10m vector wind calculation does show closer distributions to the ERA5 model, despite its quantitative overestimation. On the other hand, the 10m windspeed appears to generally underestimate the ERA5 ground truth.

One of the most prominent features of the Beaufort gyre is its ability to create new ice to distribute throughout the Arctic Ocean. The Beaufort gyre is considered an ″ice nursery″ with the concentration of polynyas stretching from the Chukchi into the Beaufort Sea. The polynya area is a factory of new ice production that, in tandem with katabatic winds etc., create new ice or ″grease ice″ that eventually congeals and consolidates to thick and sometimes multi-year ice. As this ice is created along the coast during the frost onset, it is transported north to the larger Arctic

Ocean with the transpolar drift. As the frost maximum approaches, the consolidated ice is subjected to divergent, convergent and sheer stresses whose kinematics form sea ice leads.

As the ice drifts towards the north while creating leads, the leads provide heat energy from the sea ice surface to the boundary layer of the atmosphere. In these high lead prevalent areas are the high heat flux concentrations shown in our results. Still, the concentration is subject to change, depending on the clockwise or sometimes anticlockwise movement of the gyre.

*Author Contributions*

JW was the primary producer of the study, processed and analyzed all the data and edited the manuscript.

*Competing interests*

The author declares no competing interest.

*Financial support*

This work was funded by NASA CAMEE grant#: 80NSSC19M0194.

*Acknowledgments*

We'd like to thank NASA CAMEE grant#: 80NSSC19M0194 for funding this research. Thanks to Stephen F. Ackley, Alberto M. Mestas-Nuñez, John Cassano and Grant Macdonald for their contributions to the study as well as Alexander Kurapov and the NOAA Coastal modeling seminar for accommodating discussions about the study.

## References


1. Ackley, S., Perovich, D., Maksym, T., Weissling, B., and Xie, H. (2020). Surface flooding of Antarctic summer sea ice. Annals Of Glaciology, 61(82), 117-126. doi: 10.1017/aog.2020.22.

2. Bourassa, M. A., Gille, S. T., Bitz, C., Carlson, D., Cerovecki, I., Clayson, C. A., Wick, G. A. (2013). High-latitude ocean and sea ice surface fluxes: Challenges for climate research. Bulletin of the American Meteorological Society, 94(3), 403–423. doi:10.1175/bams-d-11-00244.1.

3. Bröhan, D., and Kaleschke, L. (2014). A nine-year climatology of Arctic sea ice lead orientation and frequency from AMSR-E. Remote Sensing, 6(2), 1451-1475.

4. Cheng, Z., Pang, X., Zhao, X., & Tan, C. (2017). Spatio-temporal variability and model parameter sensitivity analysis of ice production in Ross Ice shelf polynya from 2003 to 2015. Remote Sensing, 9(9), 934. doi:10.3390/rs9090934.

5. Comiso, J. C. (2002). A rapidly declining perennial sea ice cover in the Arctic. *Geophysical Research Letters*, *29*(20). doi:10.1029/2002gl015650.

6. Dai, L., Xie, H., Ackley, S. F., and Mestas-Nuñez, A. M. (2020). Ice Production in Ross Ice Shelf Polynyas during 2017–2018 from Sentinel–1 SAR Images. *Remote Sensing*, *12*(9), 1484.

7. Delille, B., Vancoppenolle, M., Geilfus, N. X., Tilbrook, B., Lannuzel, D., Schoemann, V., Becquevort, S., Carnat, G., Delille, D., Lancelot, C. and Chou, L., Diekmann, G., and Tison, J. L. (2014). Southern Ocean CO2 sink: The contribution of the sea ice. *Journal of Geophysical Research: Oceans*, *119*(9), 6340-6355.

8. Gosink, T. A., Pearson, J. G., and Kelley, J. J. (1976). Gas movement through sea ice. *Nature*, *263*(5572), 41-42.

9. Hutchings, J., Geiger, C. A., Roberts, A., Richter-Menge, J. A., Doble, M., Forsberg, R., Giles K, Haas C, Hendricks S, Khambhamettu C, Laxon S., Martin, T., Pruis, M., Thomas M., Wadhams, P., and Zwally, H. J. (2008). *Role of ice dynamics in the sea ice mass balance*. Washington, D.C.: American Geophysical Union.

10. Lemke, P., Ren, J., Alley, R. B., Allison, I., Carrasco, J., Flato, G., Fujii, Y., Kaser, G., Mote, P., Thomas, R.H. and Zhang, T. (2007). Observations. Changes in Snow, Ice and Frozen Ground. Chapter 4.

11. Li, X., Krueger, S. K., Strong, C., Mace, G. G., and Benson, S. (2020). Midwinter Arctic leads form and dissipate low clouds. Nature Communications, 11(1), 1-8.

12. Lindsay, R., and Rothrock, D. (1995). Arctic sea ice leads from advanced very high resolution radiometer images. Journal of Geophysical Research, 100(C3), 4533. Doi: 10.1029/94jc02393.

13. Lohse, J., Doulgeris, A., and Dierking, W. (2019). An Optimal Decision-Tree Design Strategy and Its Application to Sea Ice Classification from SAR Imagery. Remote Sensing, 11(13), 1574. Doi: 10.3390/rs11131574.

14. Lohse, J., Doulgeris, A. P., and Dierking, W. (2020). Mapping sea-ice types from Sentinel-1 considering the surface-type dependent effect of incidence angle. *Annals of Glaciology*, *61*(83), 260-270.

15. Lohse, J., Doulgeris, A. P., and Dierking, W. (2021). Incident angle dependence of Sentinel-1 texture features for sea ice classification. *Remote Sensing*, *13*(4), 552.

16. Macdonald, G. J., Ackley, S. F., Mestas-Nuñez, A. M., and Blanco-Cabanillas, A. (2023). Evolution of the dynamics, area, and ice production of the Amundsen Sea Polynya, Antarctica, 2016–2021. *The Cryosphere*, *17*(2), 457-476.

17. Marcq, S., and Weiss, J. (2012). Influence of sea ice lead-width distribution on turbulent heat transfer between the ocean and the atmosphere. The Cryosphere, 6(1), 143-156. doi: 10.5194/tc-6-143-2012.

18. Martin, S. (2019). Ocean Interfaces & Human Impacts (3rd ed., Vol. 6, pp. 175–180). essay, San Diego, California: Elsevier Science.

19. Maykut, G. A. (1982). Large-scale heat exchange and ice production in the central Arctic. Journal of Geophysical Research: Oceans, 87(C10), 7971-7984.

20. Miao, X., Xie, H., Ackley, S. F., and Zheng, S. (2016). Object-based arctic sea ice ridge detection from high-spatial-resolution imagery. IEEE Geoscience and Remote Sensing Letters, 13(6), 787-791.

21. Parkinson, C. L., and Cavalieri, D. J. (2002). A 21 year record of Arctic Sea-ice extents and their regional, seasonal and monthly variability and Trends. *Annals of Glaciology*, *34*, 441–446. doi:10.3189/172756402781817725.

22. Perovich, D. (1996). The Optical Properties of Sea Ice [Ebook]. Philadelphia: US Army Corps of Engineers: Cold Regions Research and Engineering Laboratory.

23. Perovich, D. (2002). Seasonal evolution of the albedo of multiyear Arctic sea ice. Journal Of Geophysical Research, 107(C10). doi: 10.1029/2000jc000438.

24. Rösel, A., and Kaleschke, L. (2011). Comparison of different retrieval techniques for melt ponds on Arctic sea ice from Landsat and MODIS satellite data. Annals Of Glaciology, 52(57), 185-191. doi: 10.3189/172756411795931606.

25. Röhrs, J., and Kaleschke, L. (2012). An algorithm to detect sea ice leads by using AMSR-E passive microwave imagery. The Cryosphere, 6(2), 343-352. Doi: 10.5194/tc-6-343-2012.

26. Rothrock, D., Yu, Y., and Maykut, G. (1999). Thinning of the Arctic Sea-ice cover. *Geophysical Research Letters*, *26*(23), 3469–3472. doi:10.1029/1999gl010863.

27. Scharien, R. K., Segal, R., Nasonova, S., Nandan, V., Howell, S. E., and Haas, C. (2017). Winter Sentinel-1 backscatter as a predictor of spring Arctic sea ice melt pond fraction. *Geophysical Research Letters*, *44*(24), 12-262.

28. Talley, L. D. (2011). Descriptive physical oceanography: an introduction. Academic press.

29. Tschudi, M., Maslanik, J., and Perovich, D. (2008). Derivation of melt pond coverage on Arctic sea ice using MODIS observations. Remote Sensing Of Environment, 112(5), 2605-2614. doi: 10.1016/j.rse.2007.12.009.

30. Tucker, W. B., Weatherly, J. W., Eppler, D. T., Farmer, L. D., and Bentley, D. L. (2001). Evidence for rapid thinning of sea ice in the Western Arctic Ocean at the end of the 1980s. *Geophysical Research Letters*, *28*(14), 2851–2854. doi:10.1029/2001gl012967.

31. Wadhams, P., and Davis, N. R. (2000). Further evidence of ice thinning in the Arctic Ocean. *Geophysical Research Letters*, *27*(24), 3973–3975. doi:10.1029/2000gl011802.

32. Willmes, S., Bareiss, J., Haas, C., and Marcel Nicolaus. (2006). The importance of diurnal processes for the seasonal cycle of sea-ice microwave brightness temperatures during early summer in the Weddell Sea, Antarctica. *Annals of Glaciology*, *44*, 297–302. doi:10.3189/172756406781811817.

33. Willmes, S. and Heinemann, G. (2015). Sea-Ice Wintertime Lead Frequencies and Regional Characteristics in the Arctic, 2003–2015. Remote Sensing, 8(1), 4. doi: 10.3390/rs8010004.

34. Yang, M., Qiu, Y., Huang, L., Cheng, M., Chen, J., Cheng, B., & Jiang, Z. (2023). Changes in sea surface temperature and sea ice concentration in the Arctic Ocean over the past two decades. *Remote Sensing*, *15*(4), 1095. doi:10.3390/rs15041095.

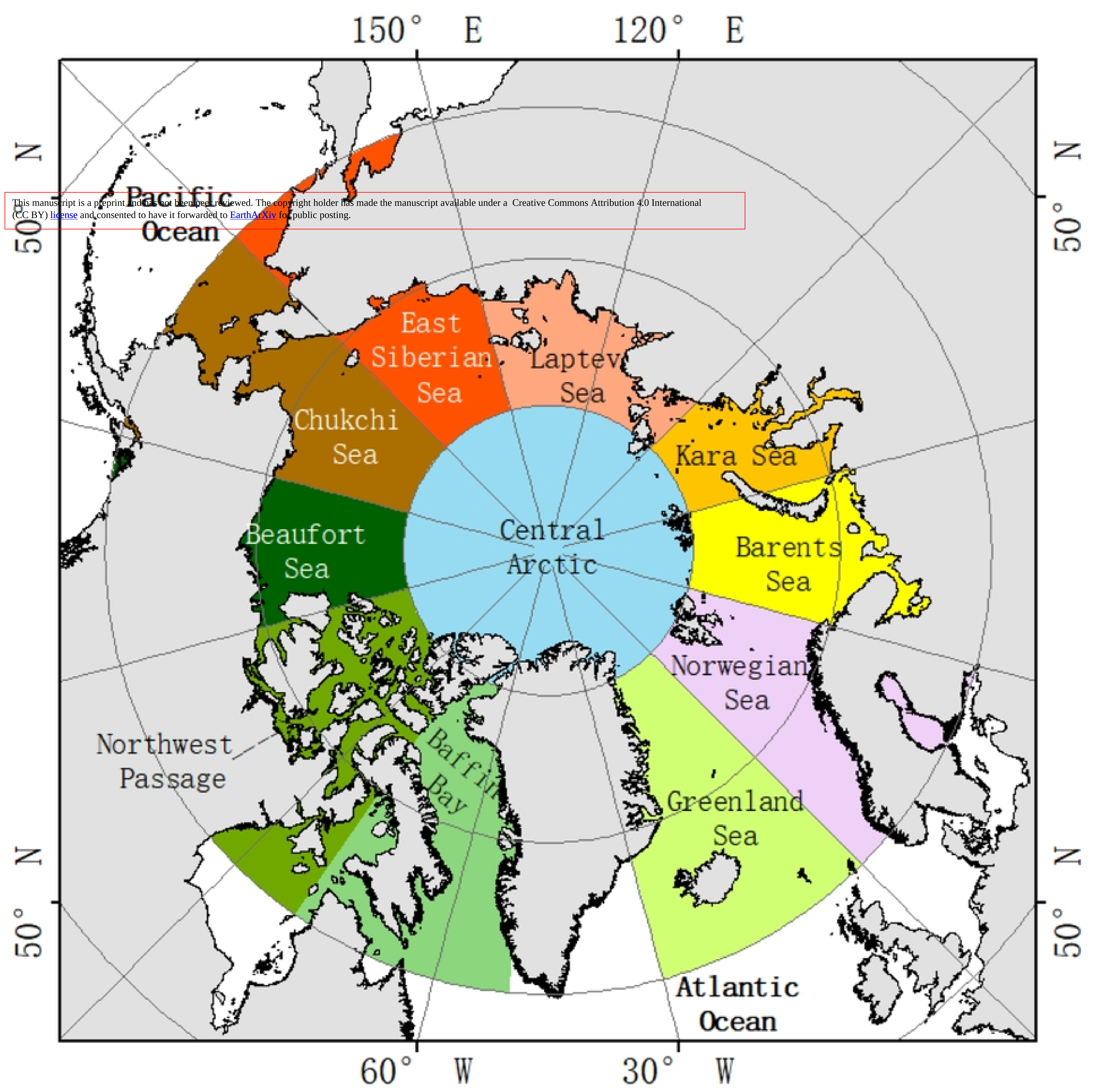

150° E
120° E
50° N
50° N
Pacific
Ocean
East
Siberian
Sea
Laptev
Sea
Chukchi
Sea
Kara Sea
Beaufort
Sea
Central
Arctic
Barents
Sea
Norwegian
Sea
Northwest
Passage
Baffin
Bay
Greenland
Sea
50° N
50° N
Atlantic
Ocean
60° W
30° W


Figure1

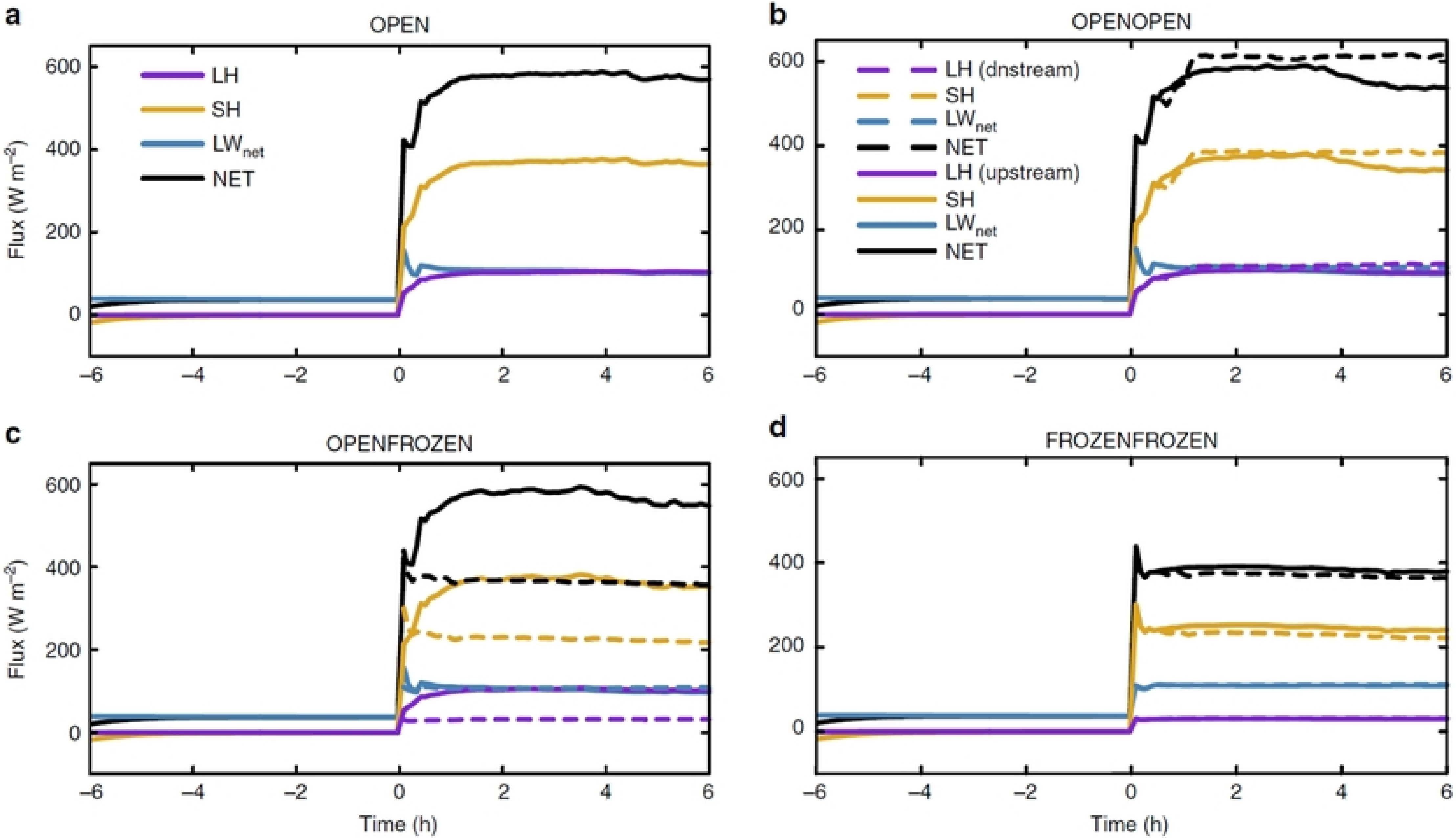
a
OPEN
b
OPENOPEN
c
OPENFROZEN
d
FROZENFROZEN
LH
SH
LWnet
NET
LH (dnstream)
SH
LWnet
NET
LH (upstream)
SH
LWnet
NET
Flux (W m−2)
Time (h)
600
400
200
0
−6
−4
−2
0
2
4
6

Figure2

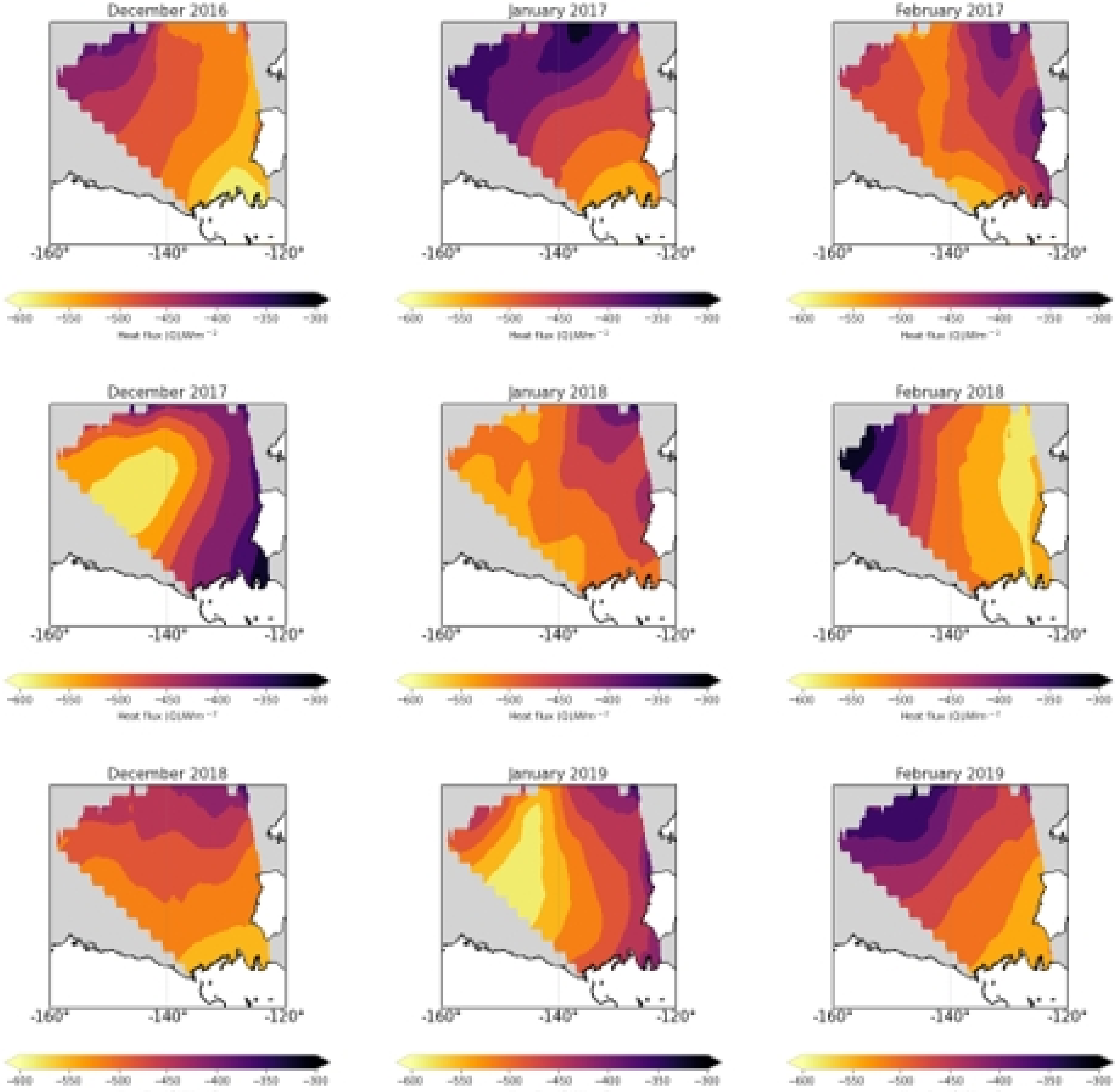

December 2016
January 2017
February 2017
December 2017
January 2018
February 2018
December 2018
January 2019
February 2019
-160°
-140°
-120°
-600
-550
-500
-450
-400
-350
-300


Figure3

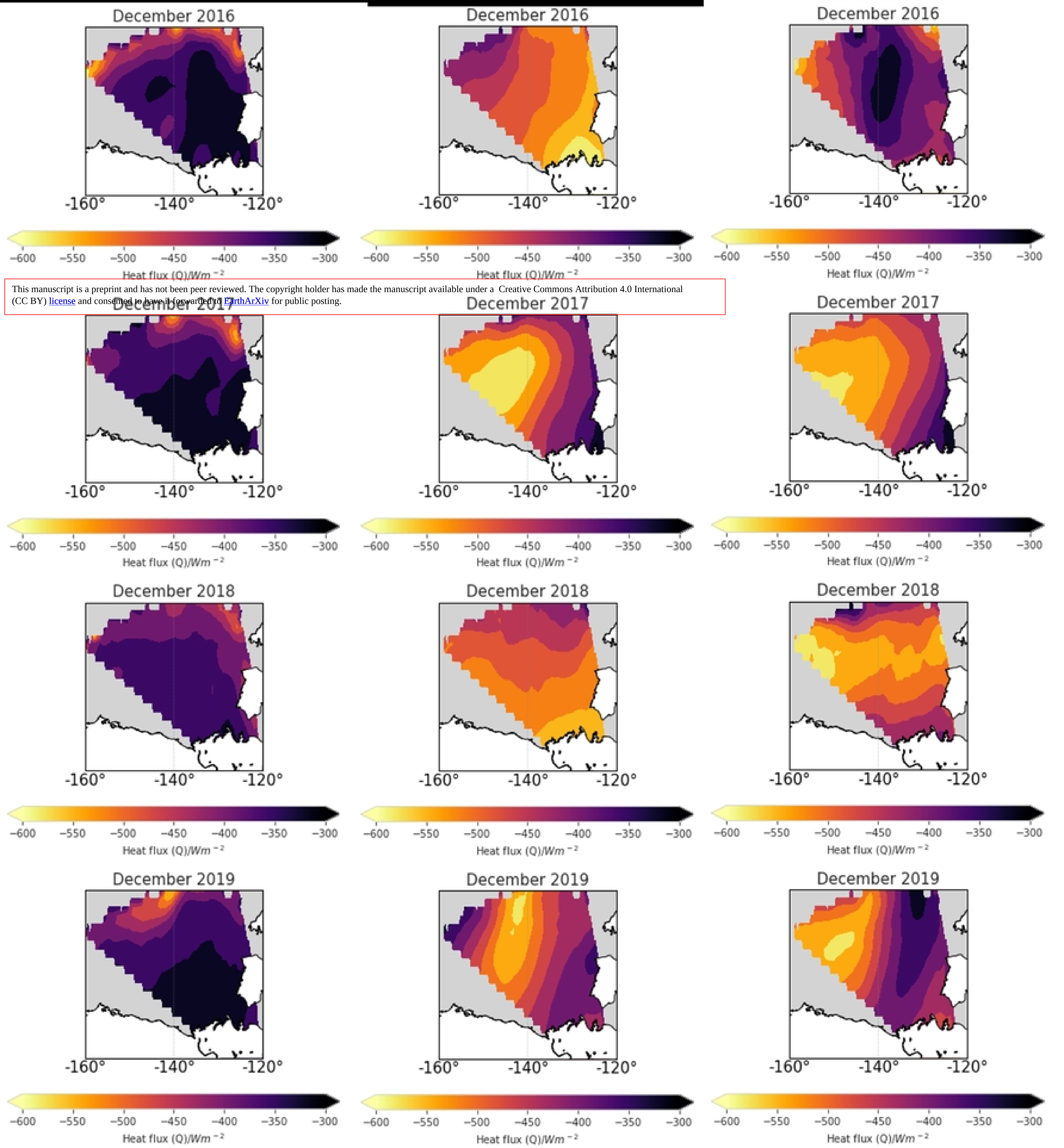
December 2016
December 2016
December 2016
December 2017
December 2017
December 2017
December 2018
December 2018
December 2018
December 2019
December 2019
December 2019
-160°
-140°
-120°
−600
−550
−500
−450
−400
−350
−300
Heat flux (Q)/Wm $^{-2}$



Figure4a

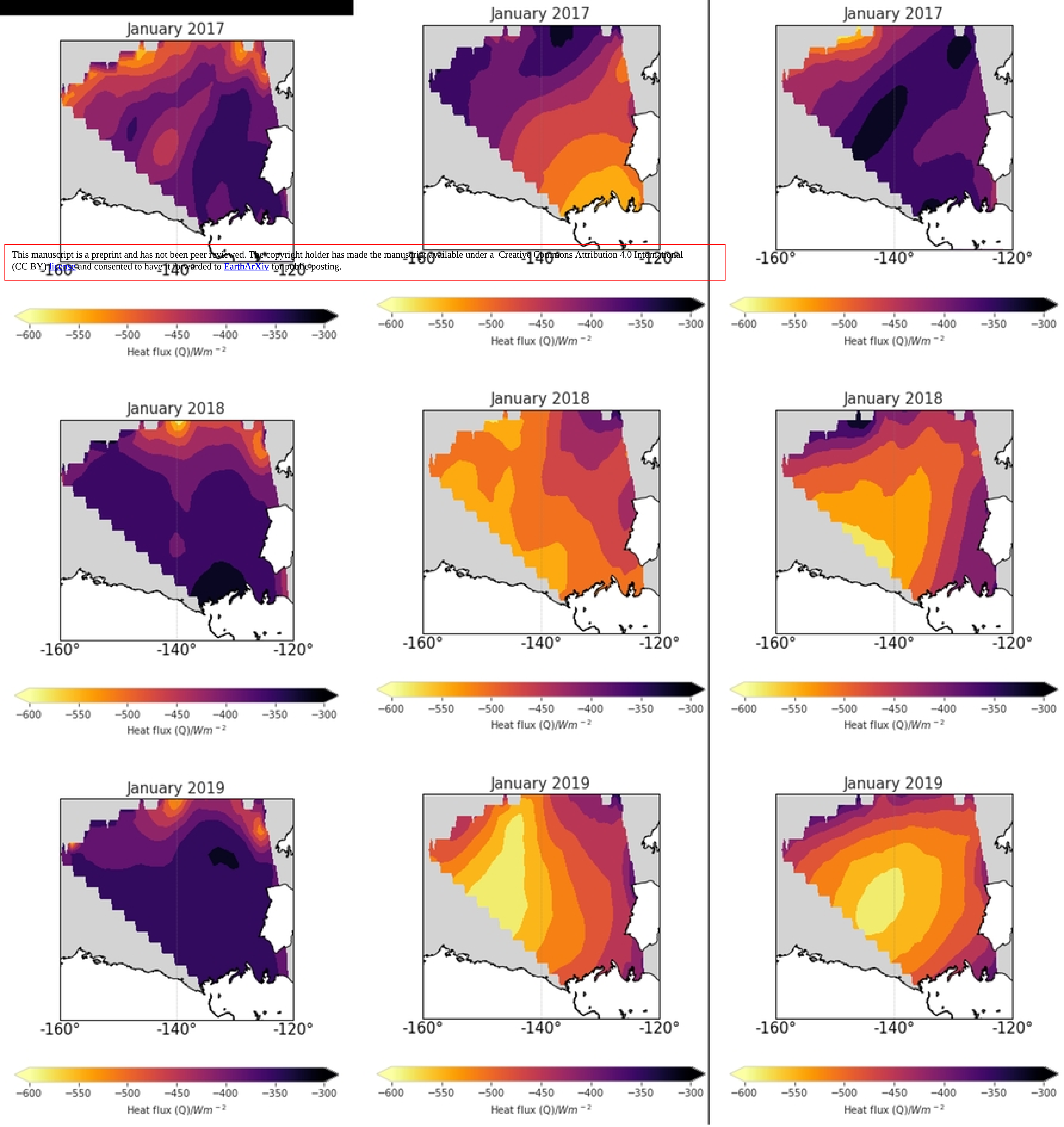

January 2017
January 2017
January 2017
January 2018
January 2018
January 2018
January 2019
January 2019
January 2019
-160°
-140°
-120°
−600
−550
−500
−450
−400
−350
−300
Heat flux (Q)/$Wm^{-2}$




Figure4b

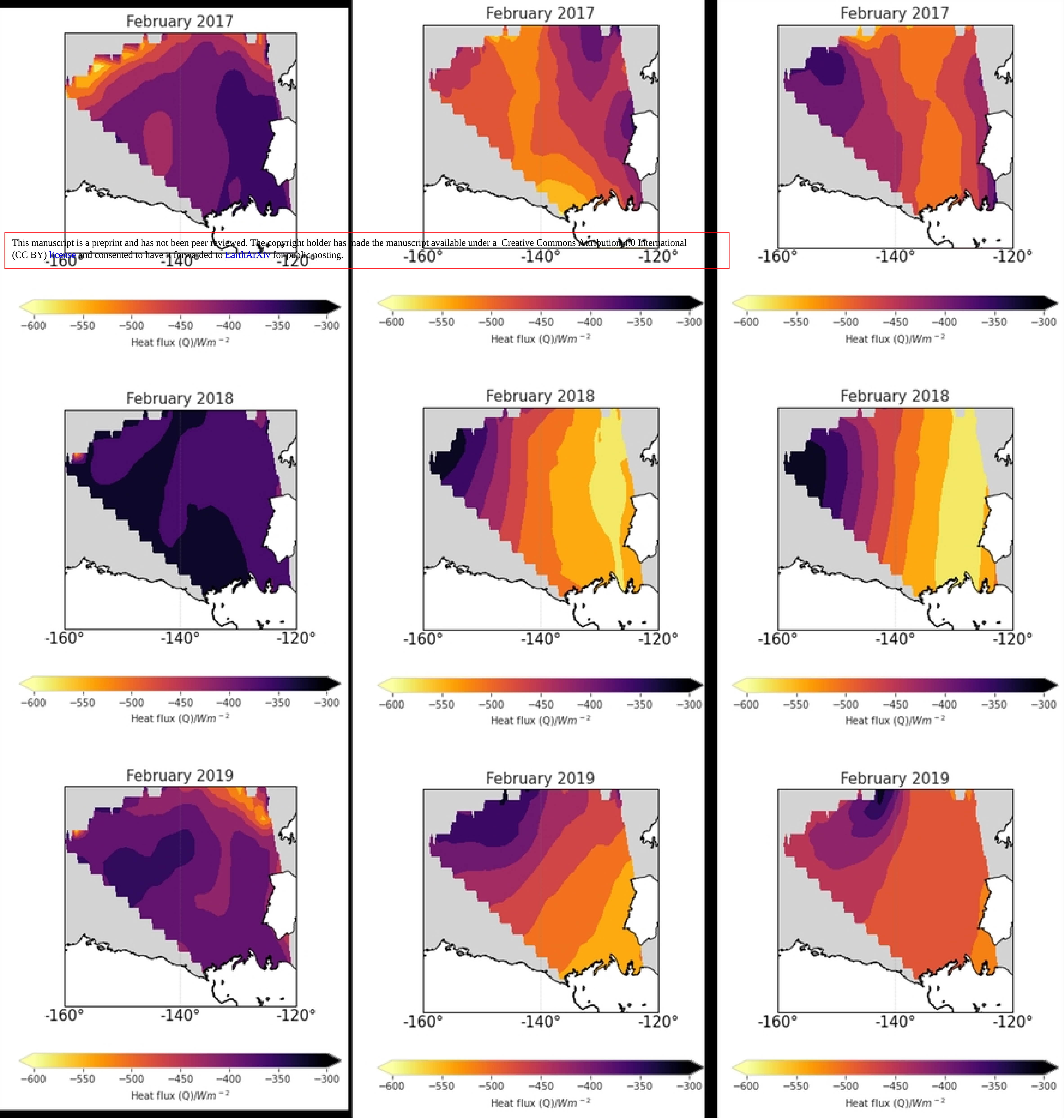
February 2017
-160°
-140°
-120°
−600 −550 −500 −450 −400 −350 −300
Heat flux (Q)/Wm −2
February 2017
-160°
-140°
-120°
−600 −550 −500 −450 −400 −350 −300
Heat flux (Q)/Wm −2
February 2017
-160°
-140°
-120°
−600 −550 −500 −450 −400 −350 −300
Heat flux (Q)/Wm −2
February 2018
-160°
-140°
-120°
−600 −550 −500 −450 −400 −350 −300
Heat flux (Q)/Wm −2
February 2018
-160°
-140°
-120°
−600 −550 −500 −450 −400 −350 −300
Heat flux (Q)/Wm −2
February 2018
-160°
-140°
-120°
−600 −550 −500 −450 −400 −350 −300
Heat flux (Q)/Wm −2
February 2019
-160°
-140°
-120°
−600 −550 −500 −450 −400 −350 −300
Heat flux (Q)/Wm −2
February 2019
-160°
-140°
-120°
−600 −550 −500 −450 −400 −350 −300
Heat flux (Q)/Wm −2
February 2019
-160°
-140°
-120°
−600 −550 −500 −450 −400 −350 −300
Heat flux (Q)/Wm −2



Figure4c

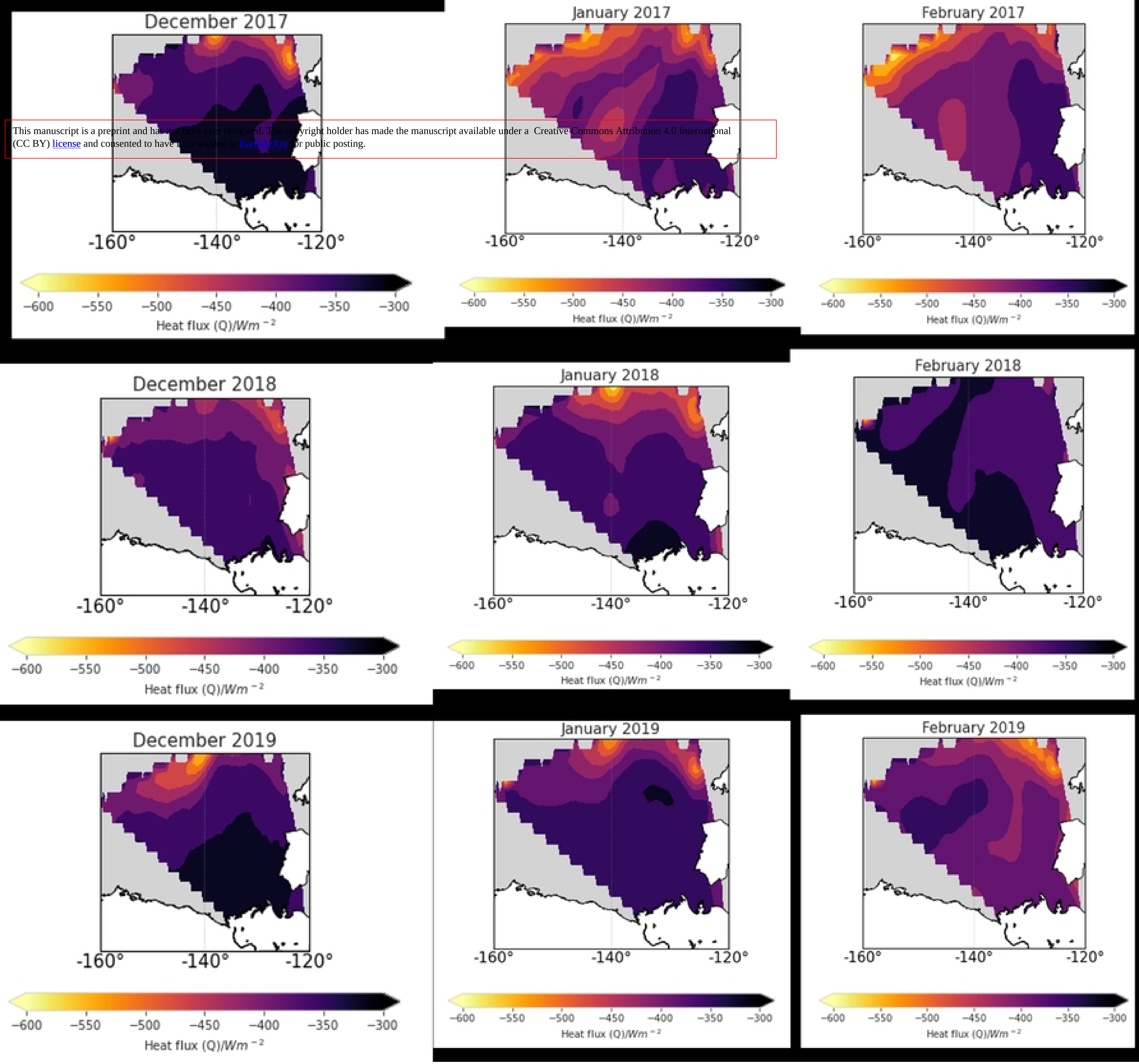
December 2017
January 2017
February 2017
December 2018
January 2018
February 2018
December 2019
January 2019
February 2019
-160°
-140°
-120°
−600
−550
−500
−450
−400
−350
−300
Heat flux (Q)/$Wm^{-2}$



Figure5